Author/s:
Wen, D;Cadusch, JJ;Meng, J;Crozier, KB

Title:
Vectorial holograms with spatially continuous polarization distributions

Date:
2021-02-24

Citation:
Wen, D., Cadusch, J. J., Meng, J. & Crozier, K. B. (2021). Vectorial holograms with spatially continuous polarization distributions. Nano Letters, 21 (4), pp.1735-1741. https://doi.org/10.1021/acs.nanolett.0c04555.

Persistent Link:
https://hdl.handle.net/11343/294849

Vectorial Holograms with Spatially-Continuous Polarization Distributions

Dandan Wen[†], Jasper J. Cadusch[†], Jiajun Meng[†], and Kenneth B. Crozier[†,‡,§]

[†]Department of Electrical and Electronic Engineering, University of Melbourne, Victoria 3010, Australia
[‡]School of Physics, University of Melbourne, Victoria 3010, Australia
[§]Australian Research Council (ARC) Centre of Excellence for Transformative Meta-Optical Systems, University of Melbourne, Victoria 3010, Australia

E-mail: kcrozier@unimelb.edu.au

Abstract

Metasurface-based holography presents opportunities for applications that include optical displays, data storage, and optical encryption. Holograms that control polarization are sometimes referred to as vectorial holograms. Most studies on this topic have concerned devices that display different images when illuminated with different polarization states. Fewer studies have demonstrated holographic images whose polarization varies spatially, i.e. as a function of position within the image. Here, we experimentally demonstrate a vectorial hologram that produces an image with a spatially-continuous distribution of polarization states, for the first time to our knowledge. An unlimited number of polarization states can be achieved within the image. Furthermore, the holographic image and its polarization map (polarization vs position in image) are independent. The same image can be thus encoded with different polarization maps. As far as we know, our approach is conceptually new. We anticipate that it could broaden the application scope of metasurface holography.

Keywords: metasurface, vectorial hologram, polarization, spatially-continuous

Introduction

Metasurfaces have proven a flexible platform for the control of optical fields[1-4]. The topic of wavefront shaping has been pursued with much interest via plasmon resonance-type[5], Mie resonance-type[6, 7] and geometric phase-type[8-11] metasurface holograms, with intended applications that include data storage[12], information processing[13], and optical encryption[14]. Geometric phase is obtained when the incident circularly polarized light is converted to its opposite helicity[15], while dispersion phase is usually achieved through surface plasmon resonances, Mie-type resonances or wave propagation[16]. Another topic that has been pursued is that of polarization control. Many of the metasurfaces developed for polarization control have been designed to manipulate the polarization states of laser beams. These devices have included polarization rotators[17], beam splitters[18], waveplates[19], and arbitrary vector beam generators[20]. Studies have also been performed on metasurfaces that generate holographic images in which polarization varies as a function of position. This has been shown in previous work but, as we

discuss below, with important limitations. This previous work can be summarized as follows. Long before the term 'metasurface' was introduced, researchers demonstrated holographic images with non-uniform polarization distributions. Lohmann[21] proposed that two orthogonally polarized reference beams could be used to interfere with the object wave and produce two independent interference patterns. When illuminated by the original pair of reference beams, the two holograms would produce a holographic image with the intensity and polarization of the target object. The use of a photo-anisotropic material as the recording medium has also been studied, with the polarization state being physically recorded by the material becoming optically anisotropic when exposed to polarized light[22]. Further progress has accompanied the introduction of the metasurface concept. The most straightforward case is the two channel hologram which simultaneously reconstructs left and right circularly-polarized images (LCP and RCP, [9, 23-26]), or *x*- and *y*-polarized images[27-30]. The work of Deng et al increased the number of channels via diatomic metasurfaces in which each unit cell consisted of two orthogonal meta-atoms[31]. The latter comprised silver antennas formed above a silver mirror (with an SiO_2 spacer). By adjusting the position and orientation angle of the antennas within a unit cell, phase and polarization control could be achieved. A single holographic image containing four polarization states was demonstrated. Song et al adopted phase gradient supercells to simultaneously provide phase and polarization control for the transmitted light. Four separate images with different polarization states were realized[32]. Zhao et al used birefringent metasurfaces to realize multichannel vectorial holograms[33]. The metasurface was composed of rectangular-shaped silicon antennas whose geometry and orientation were spatially modulated to provide three holographic phase profiles. Different holographic images could be produced by controlling the input/output polarization combination. Similar principles were used for multicolor holograms with red, green and blue images corresponding to different polarization channels[34]. Although these works successfully demonstrate the concept of vectorial holography, the maximum number of polarization states in the generated holographic image was four (*x*-polarized, *y*-polarized, LCP and RCP). For some applications, e.g. optical document security, the ability to generate holographic images with an unlimited number of polarization states would be advantageous. In this paper, we demonstrate this capability.

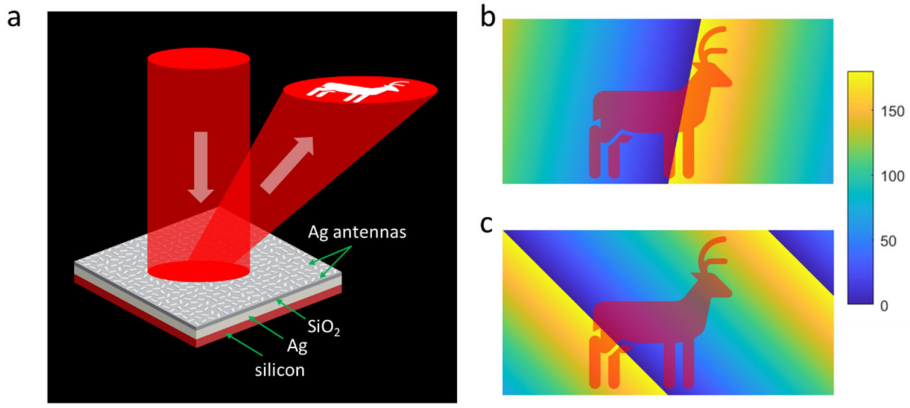

Figure 1. Schematic illustration of metasurface that generates holographic pattern with continuous polarization distribution. a) Illumination is at normal incidence, with reflected beam containing vectorial holographic image. b-c) Same holographic image (deer pattern) can be made to have different polarization maps by slight adjustment of supercell structure of metasurface. Here, the blue-yellow colormap denotes polarization direction, with 0°/90° representing horizontal/vertical polarizations.

To address this challenge, we experimentally demonstrate a vectorial hologram that produces a holographic image with a spatially-continuous polarization distribution. The concept is shown in Figure 1a. Illumination is linearly polarized and at normal incidence, with the holographic image (here a deer pattern) produced as an off-axis reflected beam. Example polarization maps are schematically shown as Figure 1b, with the colors denoting the polarization direction, which varies continuously across the pattern. With different design parameters, the same intensity pattern can be encoded with different polarization maps (Figure 1b-c). By the same token, the same polarization map can be encoded into different intensity patterns. The physical mechanism underlying the design principle we introduce in this paper and the nature of the reflection-type plasmonic metasurface we employ enable us to demonstrate operation over a wide range of wavelengths, from the green to the near infrared (NIR). This broad bandwidth would be advantageous for many applications.

Results

Figure 1a provides a schematic illustration of the metasurface, which consists of a silver mirror layer on a silicon substrate, an SiO_2 spacer and an array of rectangular silver nanorods. We choose silver because its absorption in our intended wavelength range (visible to NIR) is not excessive. Due to an interplay between localized surface plasmons (on the nanorods) and Fabry-Pérot effects in this multilayer structure, each nanorod can function as a half-wave plate[8]. When illuminated with circularly-polarized light, part of the reflected light will preserve the handedness of the incident light and a geometric phase of 2φ will be imparted, where φ denotes the orientation angle of the nanorod.

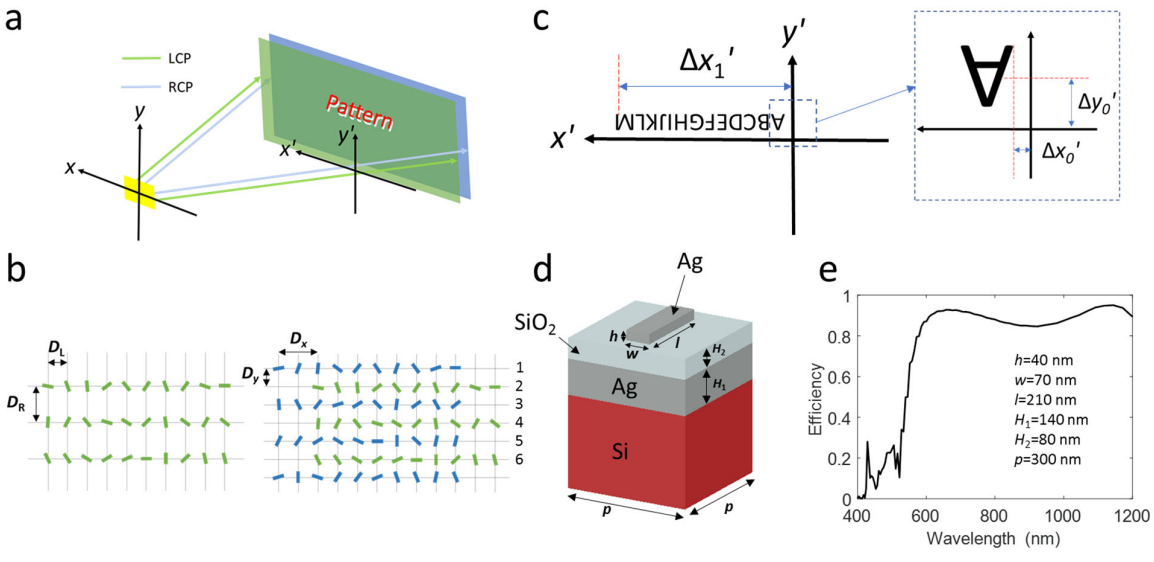

Figure 2. Design principle of our vectorial holography approach, schematic of unit cell, and simulated conversion efficiency. (a) Schematic of our method. LCP and RCP beams reflected from metasurface form two identical holographic images, but with spatially-continuous phase difference. (b) Schematic of metasurfaces before (left panel) and after (right panel) interleaving process. (c) Target image used in this paper, which consists of letters 'A' to 'M'. (d) Schematic of unit cell of metasurface. (e) Simulated conversion efficiency of unit cell. Geometrical parameters are labeled. Incident light is assumed to be LCP, and conversion efficiency is defined as power of LCP reflected light divided by that of incident light.

We next describe the design principle we employ in our metasurface to achieve a continuously-varying polarization distribution. Consider that the target holographic image is the word 'pattern' (Figure 2a). A phase-only hologram Φ_A corresponding to this image is generated with the Gerchberg-Saxton algorithm[35]. The pixels of Φ_A are arranged in a rectangular lattice with M rows and N columns. The column spacing and the row spacing are denoted as D_L and D_R, respectively. We encode Φ_A by an array of silver nanorods, where a pixel with phase value φ_j is represented by a nanorod with the orientation angle $-\varphi_j/2$. This is illustrated by the green nanorods in the left panel of Figure 2b. These nanorods are symmetrically inverted about the vertical axis and replicated in a new location defined by the vector (D_x, D_y) in the xy plane. The new (i.e. replicated) nanorods are colored with blue, as shown in the right panel of Figure 2b. The two types of nanorods (green and blue) together form a new metasurface, and two neighboring rows form a supercell (rows 1 and 2 for example).

If the incident light is LCP, it will be converted by the green nanorods to form an LCP holographic pattern in the designed observation area ($y' > 0$ for the example shown in Figure 2a). Similarly, the RCP light is converted by the blue nanorods to form the same pattern, but with RCP light. Since green and blue nanorods have displacement (D_x, D_y), a coordinate-related phase difference between LCP and RCP images in $x'y'$ plane will be generated[36]. As derived in Supplementary Note 1, this is given by:

$$\phi(x', y')_{LCP-RCP} = 2\pi \left(D_x \frac{x'}{\lambda \Delta z} + D_y \frac{y'}{\lambda \Delta z} \right) \quad (1)$$

where Δz is the propagation distance between the metasurface and the observation plane. When the incident light is x-polarized, which contains equal LCP/RCP components and zero phase difference, the holographic image will be a superposition of LCP and RCP images with $\phi(x', y')_{LCP-RCP}$. As a result, the polarization direction (denoted by the angle formed by the electric field vector and x' axis) of the combined holographic image varies with position (i.e. coordinates (x', y')) according to[17]

$$\theta(x', y') = \frac{\phi(x', y')_{LCP-RCP}}{2} \quad (2)$$

Here we have a target image consisting of 13 letters that range from 'A' to 'M' (Figure 2c). The polarization of the image is designed to change gradually from horizontal polarization (along x'

direction) to vertical polarization (along y' direction) from 'A' to 'M'. The image is designed to be long and narrow, which means that the coordinate range in the y' direction is much smaller than that in the x' direction. As a result, the second term on the right side of Equation (1) varies over a much smaller range of values than does the first term. Therefore, while there is variation of polarization along the y' direction, it is quite minor compared to that along the x' direction. We therefore focus only on the polarization in the x' direction. As shown in Figure 2c, we use

$$\phi(\Delta x_0', \Delta y_0')_{LCP-RCP} = 2\pi\left(C_1 D_x + C_2 D_y\right) = 0 \tag{3}$$

$$\phi(\Delta x_1', \Delta y_0')_{LCP-RCP} = 2\pi\left(C_3 D_x + C_2 D_y\right) = -\pi \tag{4}$$

From Equation (2), it follows that the right edge of 'A' [coordinates $(\Delta x_0', \Delta y_0')$] and the left edge of 'M' [coordinates $(\Delta x_1', \Delta y_0')$] will have polarization directions of 0 and -π/2, respectively. The part of the image between 'A' and 'M' will gradually change from 0 to -π/2. In this paper, we have D_x = -1500 nm, D_y = 300 nm, $C_1 = 3.33\times10^4$, $C_2 = 1.67\times10^5$, and $C_3 = 3.67\times10^5$. It is worth noting that, to realize the same vectorial holographic image, there are many different choices for (C_1, C_2, C_3) with D_x and D_y fixed. The choice of (C_1, C_2, C_3) governs the position of the holographic image in the observation plane. Further discussion on this point is provided in Supplementary Note 2. In Equations (3)-(4), the coordinate-related phase difference is confined to be between -π to 0, however, we can change the value of (C_1, C_2, C_3), D_x and D_y to achieve a 2π phase coverage. This would then allow the generated image to have all the possible linear polarization directions (0 to π). Figure 2d shows a unit cell of the metasurface. Here we optimize the geometric parameters of a unit cell (h, w, l, H_1, H_2, p) with the goal of high efficiency in visible to NIR spectral range. The parameters of the unit cell we choose, and the simulated conversion efficiency, are shown in Figure 2e. More analysis on the efficiency and phase modulation function of a unit cell can be found in Supplementary Note 3. Fabrication details and SEM image of the metasurface are provided in Supplementary Note 4. As shown in Figure 3a, the metasurface is mounted on a three-axis translation stage to position it in the set-up. A horizontally-polarized (parallel to x-axis as in Figure 2a) laser beam illuminates the metasurface (located at z=0) at normal incidence. The reflected holographic image passes through a polarizer (Thorlabs LPVISE100-A) at z = 17.5 cm, and illuminates a paper screen (at z = 62 cm). A camera is placed at a distance of 32.5 cm from this screen. The red (Thorlabs CPS 635, $\lambda = 635\ nm$) and green (Thorlabs CPS 532, $\lambda = 532\ nm$) laser beams are collimated to approximate plane wave illumination. With the polarizer (denoted "P" in Figure 3a) removed, clear holographic images can be observed (Figure 3b). Here we rotate the image by 180° for convenience.

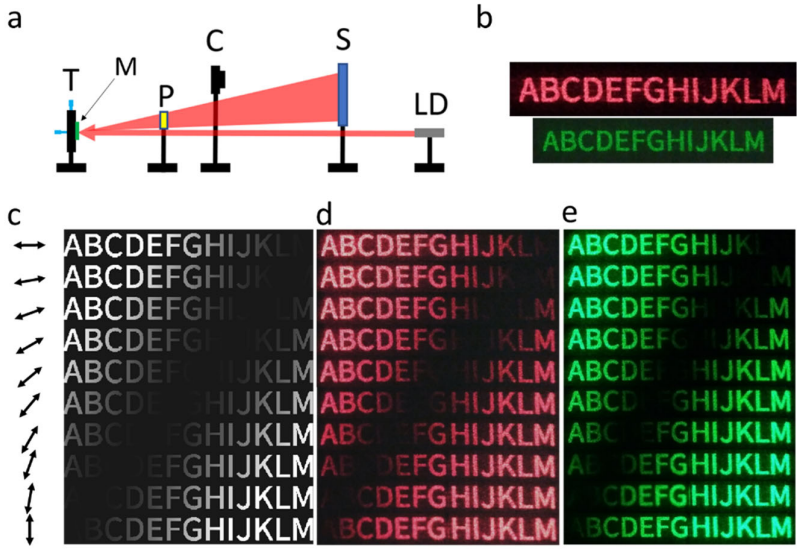

Figure 3. Experimental setup and holographic images. (a) Schematic of experimental setup. T: translation stage. M: metasurface. P: polarizer. C: camera. S: screen. LD: laser diode. (b) Holographic images generated by illumination with lasers with wavelengths of 635 nm and 532 nm. Widths of red and green holographic images (from left edge of 'A' to the right edge of 'M') are 13.2 cm and 11 cm, respectively. (c) Simulated holographic images obtained for different polarization directions of analyzing polarizer. Images from top to bottom are for polarizer direction varying from 0° (horizontal direction) to 90° (vertical direction) in steps of 10°. Arrows on left side denote polarizer direction. (d)-(e) Experimental results obtained for red ($\lambda = 635\ nm$) and green ($\lambda = 532\ nm$) light.

We next use an analyzing polarizer (P in Figure 3a) to verify the polarization state distribution in the holographic image. The diameter of the polarizer (2.54 cm) is insufficient to span the entire holographic image. We thus obtain each image using two steps. The first step, the polarizer covers the letters 'A' to 'G'. We then translate the polarizer so that in the second step it covers the letters 'H' to 'M'. The two images are the combined. Figure 3a shows the simulated results, where we add the LCP and RCP target images that differ in phase by the detour phase of Equation 1. When the analyzing polarizer direction is rotated anticlockwise from horizontal to vertical (as denoted by arrows on left side of Figure 3c), the dark area translates from the 'M'- to the 'A'-side of the image. In Figure 3d-e, we present the experimental results obtained with red (635 nm) and green (532 nm) laser beams. It can be seen that the results are in good agreement with the simulation, which is consistent with the polarization changing from horizontal to vertical across the letters 'A' to 'M'.

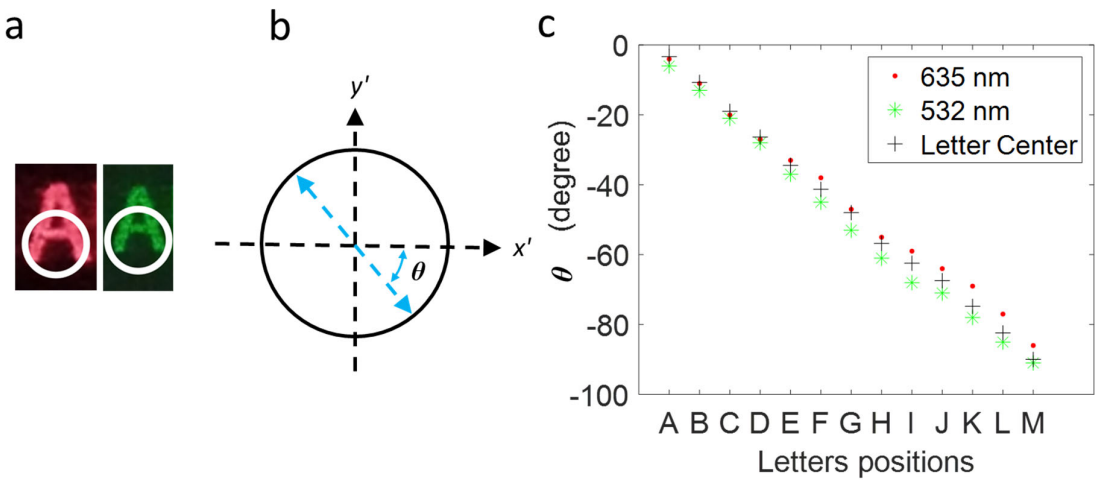

Figure 4. Polarization states of different letters. (a) White circle on letter 'A' denotes photosensitive region of power meter, which has a diameter of 0.95 cm. Letter 'A' has widths of 1.1 cm and 0.92 cm for red and green images, respectively. (b) Schematic of polarization direction θ, with blue dashed arrow denoting electric field vector of linearly polarized light. (c) Experimentally measured θ of different letters for red (635 nm) and green (532 nm) illumination. Black crosses show theoretical value of polarization direction at center of each letter, calculated using Equations 1 and 2.

We next study the polarization state as a function of position within the image, i.e. of different letters. We replace the paper screen by a power meter (Thorlabs PM100D) at the same position. We begin by positioning the power meter so that it is centered over the letter 'A' in the horizontal direction and is low enough (in the vertical direction) so that the bottom edge of the letter is enclosed (Figure 4a). We then rotate the analyzing polarizer to find the angle at which the transmitted power is maximized. This corresponds to the polarization direction θ (Figure 4b). Next, we translate the power meter to measure the polarization direction of letters 'B', 'C' and up to 'M' (Figure 4c, red dots and green asterisks). For comparison, in Figure 4c (black crosses) we plot the polarization direction expected from theory (Eqns 1 and 2). For convenience, we use the center of the letter as the reference point. For example, the letter 'A' occupies a rectangular area with the bottom left corner (x_0', y_0') and top right corner (x_1', y_1'). It is the polarization direction at the point $(x_0'/2+x_1'/2, y_0'/2+y_1'/2)$ that is plotted in Figure 4c (black crosses). The measured results show reasonable agreement with our expectations for this design (i.e. theory).

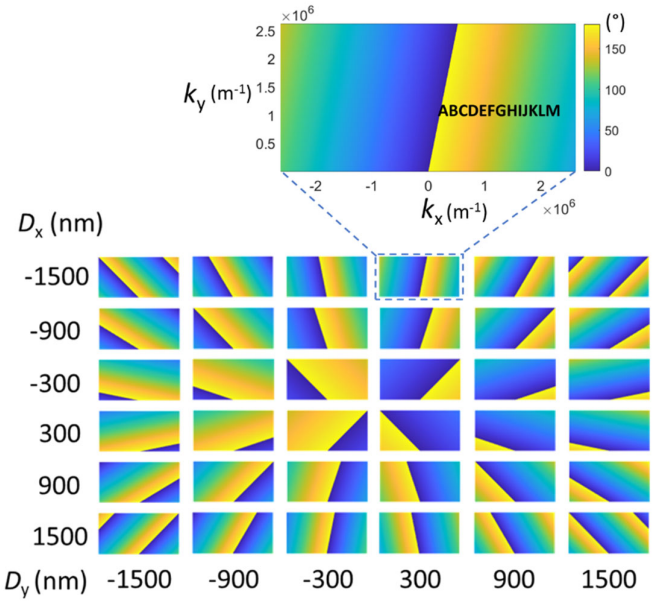

Figure 5. Polarization distributions resulting from different combinations of (D_x, D_y). Zoomed-in image corresponds to case considered in our experiment (D_x = -1500 nm and D_y = 300 nm). Letters 'A' to 'M' are indicated on polarization map. Color (blue to yellow) denotes polarization direction.

In the demonstration described above, we have D_x = -1500 nm and D_y = 300 nm. As we illustrate in Figure 5**,** however, a variety of polarization maps can be achieved for other combinations of (D_x, D_y). We note that the Fraunhofer diffraction description assumes the paraxial approximation and the calculated results thus are accurate when the absolute values of wavevector's x- and y- components (k_x and k_y) are not too large[37]. As shown in Figure 2c, our vectorial image corresponds to the +1st order of the reflected light. There will also be the -1st order beam that arises from the conjugation of the geometric phase. The polarization distribution of -1st order is the same as that of the +1st orders, i.e., a given letter (e.g. 'A') will have the same polarization in the -1st order as it does in the +1st order. To avoid the two orders from overlapping, we choose to position the observation zone at $y' > 0$. As indicated in Figure 5, the observation zone is confined to the area defined by $|k_x| = |2\pi x'/\lambda\Delta z| < 2.5\times10^6$ and $0 < k_y\ (= 2\pi y'/\lambda\Delta z) < 2.5\times10^6$. For λ= 635 nm, this corresponds to the field of view spanning from -14.6° to 14.6° in the x-direction, and from 0° to 14.6° in the y-direction. In addition to the linear polarization distribution shown in Figure 5, it is possible to generate holographic images with other polarization states (such as elliptical and circular polarization) with the method we demonstrate here (see Supplementary Note 5).

We have previously shown that the Ag-SiO_2-Ag structure[23] has broadband performance that covers the visible to NIR range. Here we employ the interleaving method to produce the metasurface hologram. This results in multiple diffraction orders, and thus lower the efficiency. A detailed discussion on this point can be found in Supplementary Note 6. The efficiency is defined as the power in the ±1st diffraction orders divided by that of the incident light. We use a supercontinuum laser as the light source (SuperK COMPACT). The illumination spot is smaller than the metasurface extent.

We position the metasurface so that it is illuminated at normal incidence. The $\pm 1^{st}$ order beam is collected by another lens (f= 10 cm) and measured by the power meter. The measured efficiency curve is shown in Supplementary Note 7. The efficiency is exceeds 10% over the wavelength range 570 nm to 1025 nm, which is higher than[31], or comparable to[33], recent reports. Further information on the vectorial holographic images (at a wavelength of 850 nm) is provided in Supplementary Note 8.

There are two main advantages to using silver, rather than a dielectric, for the metasurface. The first is that fabrication is relatively straightforward. Dielectric metasurfaces usually feature high aspect ratio nanoantennas, which are generally achieved through the careful control over the reactive iron etching process. On the other hand, a silver metasurface can be realized through a one-step lift-off process. The second is that our silver metasurface can achieve high efficiency over a broad wavelength range (Figure 2e). The working wavelength ranges of dielectric metasurfaces are generally narrower[38]. One would therefore need to use several dielectric metasurfaces, each with different unit cell structures, to cover the visible to NIR range.

The design principle we employ may also benefit other applications. For example, we could use a target image containing discrete round spots (e.g. a 2D spot array) instead of the 'ABCD…' pattern demonstrated above. The position of each spot would be chosen to ensure that it has a unique polarization state. This metasurface could be used to generate multiple polarization channels[39, 40]. In another example application, the metasurface proposed here plus a CMOS image sensor could be used as a compact birefringence detector without moving parts. The vectorial holographic image would illuminate the material under study (transparent and birefringent) and then pass through an analyzing polarizer. The transmitted light would be collected by the CMOS image sensor, with direct read-out of the image enabling the birefringence of the analyte to be deduced. We anticipate that our metasurface may also be useful in optical document security[41, 42], providing a highly distinctive polarization response that is difficult to reproduce using other means.

Conclusion

In conclusion, we have demonstrated a method to generate vectorial holographic images with continuous polarization distributions. The vectorial holograms that have been previously demonstrated have had a limited number of polarization channels. Our method has an unlimited number of polarization channels while also generating holographic images. The polarization maps and the holographic images are independent, which means that same holographic image can be encoded with different polarization maps. Similarly, the same polarization map can be encoded with different holographic images. We suggest that our method could find a broad range of applications such as for the generation of multiple polarization states, for birefringence detectors, and for optical document security.

Acknowledgements

This work was supported by the Australian Research Council (DP180104141). This work was performed in part at the Melbourne Centre for Nanofabrication (MCN) in the Victorian Node of the Australian National Fabrication Facility (ANFF).

Supporting Information

This material is available free of charge via the internet at https://protect-au.mimecast.com/s/CC_5CxnMJ5s1KMWAGUYx1xu?domain=pubs.acs.org

References

1. Yu, N. F.; Genevet, P.; Kats, M. A.; Aieta, F.; Tetienne, J. P.; Capasso, F.; Gaburro, Z. Light Propagation with Phase Discontinuities: Generalized Laws of Reflection and Refraction *Science* **2011,** *334*, 333-337.
2. Li, G.; Zhang, S.; Zentgraf, T. Nonlinear photonic metasurfaces *Nat. Rev. Mater.* **2017,** *2*, 17010.
3. Chen, S.; Liu, W.; Li, Z.; Cheng, H.; Tian, J. Metasurface‐Empowered Optical Multiplexing and Multifunction *Adv. Mater.* **2020,** *32*, 1805912.
4. Deng, Z. L.; Jin, M.; Ye, X.; Wang, S.; Shi, T.; Deng, J.; Mao, N.; Cao, Y.; Guan, B. O.; Alù, A. Full‐Color Complex‐Amplitude Vectorial Holograms Based on Multi‐Freedom Metasurfaces *Adv. Funct. Mater.* **2020,** *30*, 1910610.
5. Chen, W. T.; Yang, K. Y.; Wang, C. M.; Huang, Y. W.; Sun, G.; Chiang, I. D.; Liao, C. Y.; Hsu, W. L.; Lin, H. T.; Sun, S.; Zhou, L.; Liu, A. Q.; Tsai, D. P. High-Efficiency Broadband Meta-Hologram with Polarization-Controlled Dual Images *Nano Lett.* **2014,** *14*, 225-230.
6. Wang, L.; Kruk, S.; Tang, H.; Li, T.; Kravchenko, I.; Neshev, D. N.; Kivshar, Y. S. Grayscale transparent metasurface holograms *Optica* **2016,** *3*, 1504-1505.
7. Yoon, G.; Lee, D.; Nam, K. T.; Rho, J. Pragmatic metasurface hologram at visible wavelength: the balance between diffraction efficiency and fabrication compatibility *ACS Photonics* **2017,** *5*, 1643-1647.
8. Zheng, G.; Mühlenbernd, H.; Kenney, M.; Li, G.; Zentgraf, T.; Zhang, S. Metasurface holograms reaching 80% efficiency *Nat. Nanotechnol.* **2015,** *10*, 308-312.
9. Zhang, X.; Pu, M.; Guo, Y.; Jin, J.; Li, X.; Ma, X.; Luo, J.; Wang, C.; Luo, X. Colorful metahologram with independently controlled images in transmission and reflection spaces *Adv. Funct. Mater.* **2019,** *29*, 1809145.
10. Khorasaninejad, M.; Crozier, K. B. Silicon nanofin grating as a miniature chirality-distinguishing beam-splitter *Nat. Commun.* **2014,** *5*, 1-6.
11. Bao, Y.; Yu, Y.; Xu, H.; Guo, C.; Li, J.; Sun, S.; Zhou, Z.-K.; Qiu, C.-W.; Wang, X.-H. Full-colour nanoprint-hologram synchronous metasurface with arbitrary hue-saturation-brightness control *Light Sci. Appl.* **2019,** *8*, 1-10.
12. Deng, Z.-L.; Li, G. Metasurface optical holography *Materials Today Physics* **2017,** *3*, 16-32.
13. Ren, H.; Briere, G.; Fang, X.; Ni, P.; Sawant, R.; Héron, S.; Chenot, S.; Vézian, S.; Damilano, B.; Brändli, V. Metasurface orbital angular momentum holography *Nat. Commun.* **2019,** *10*, 1-8.
14. Zhou, H.; Sain, B.; Wang, Y.; Schlickriede, C.; Zhao, R.; Zhang, X.; Wei, Q.; Li, X.; Huang, L.; Zentgraf, T. Polarization-Encrypted Orbital Angular Momentum Multiplexed Metasurface Holography *ACS nano* **2020,** *14*, 5553-5559.
15. Biener, G.; Niv, A.; Kleiner, V.; Hasman, E. Formation of helical beams by use of Pancharatnam–Berry phase optical elements *Opt. Lett.* **2002,** *27*, 1875-1877.
16. Yu, N. F.; Capasso, F. Flat optics with designer metasurfaces *Nat. Mater.* **2014,** *13*, 139-150.
17. Wen, D.; Yue, F.; Zhang, C.; Zang, X.; Liu, H.; Wang, W.; Chen, X. Plasmonic metasurface for optical rotation *Appl. Phys. Lett.* **2017,** *111*, 023102.
18. Zhu, L.; Liu, X.; Sain, B.; Wang, M.; Schlickriede, C.; Tang, Y.; Deng, J.; Li, K.; Yang, J.; Holynski, M. A dielectric metasurface optical chip for the generation of cold atoms *Sci. Adv.* **2020,** *6*, eabb6667.
19. Ding, F.; Wang, Z.; He, S.; Shalaev, V. M.; Kildishev, A. V. Broadband high-efficiency half-wave plate: a supercell-based plasmonic metasurface approach *ACS nano* **2015,** *9*, 4111-4119.

20. Arbabi, E.; Kamali, S. M.; Arbabi, A.; Faraon, A. Vectorial holograms with a dielectric metasurface: ultimate polarization pattern generation *ACS Photonics* **2019,** *6*, 2712-2718.
21. Lohmann, A. Reconstruction of vectorial wavefronts *Applied Optics* **1965,** *4*, 1667-1668.
22. Nikolova, L.; Ramanujam, P. S., *Polarization holography*. Cambridge University Press: 2009.
23. Wen, D.; Yue, F.; Li, G.; Zheng, G.; Chan, K.; Chen, S.; Chen, M.; Li, K. F.; Wong, P. W. H.; Cheah, K. W. Helicity multiplexed broadband metasurface holograms *Nat. Commun.* **2015,** *6*, 1-7.
24. Jin, L.; Dong, Z.; Mei, S.; Yu, Y. F.; Wei, Z.; Pan, Z.; Rezaei, S. D.; Li, X.; Kuznetsov, A. I.; Kivshar, Y. S. Noninterleaved metasurface for (26-1) spin-and wavelength-encoded holograms *Nano Lett.* **2018,** *18*, 8016-8024.
25. Wang, B.; Dong, F.; Yang, D.; Song, Z.; Xu, L.; Chu, W.; Gong, Q.; Li, Y. Polarization-controlled color-tunable holograms with dielectric metasurfaces *Optica* **2017,** *4*, 1368-1371.
26. Huang, L.; Mühlenbernd, H.; Li, X.; Song, X.; Bai, B.; Wang, Y.; Zentgraf, T. Broadband hybrid holographic multiplexing with geometric metasurfaces *Adv. Mater.* **2015,** *27*, 6444-6449.
27. Schonbrun, E.; Seo, K.; Crozier, K. B. Reconfigurable imaging systems using elliptical nanowires *Nano Lett.* **2011,** *11*, 4299-4303.
28. Xie, Z.; Lei, T.; Si, G.; Wang, X.; Lin, J.; Min, C.; Yuan, X. Meta-holograms with full parameter control of wavefront over a 1000 nm bandwidth *Acs Photonics* **2017,** *4*, 2158-2164.
29. Chen, W. T.; Yang, K.-Y.; Wang, C.-M.; Huang, Y.-W.; Sun, G.; Chiang, I.-D.; Liao, C. Y.; Hsu, W.-L.; Lin, H. T.; Sun, S. High-efficiency broadband meta-hologram with polarization-controlled dual images *Nano Lett.* **2014,** *14*, 225-230.
30. Arbabi, A.; Horie, Y.; Bagheri, M.; Faraon, A. Dielectric metasurfaces for complete control of phase and polarization with subwavelength spatial resolution and high transmission *Nat. Nanotechnol.* **2015,** *10*, 937-943.
31. Deng, Z.-L.; Deng, J.; Zhuang, X.; Wang, S.; Li, K.; Wang, Y.; Chi, Y.; Ye, X.; Xu, J.; Wang, G. P. Diatomic metasurface for vectorial holography *Nano Lett.* **2018,** *18*, 2885-2892.
32. Song, Q.; Baroni, A.; Sawant, R.; Ni, P.; Brandli, V.; Chenot, S.; Vézian, S.; Damilano, B.; de Mierry, P.; Khadir, S. Ptychography retrieval of fully polarized holograms from geometric-phase metasurfaces *Nat. Commun.* **2020,** *11*, 1-8.
33. Zhao, R.; Sain, B.; Wei, Q.; Tang, C.; Li, X.; Weiss, T.; Huang, L.; Wang, Y.; Zentgraf, T. Multichannel vectorial holographic display and encryption *Light Sci. Appl.* **2018,** *7*, 1-9.
34. Hu, Y.; Li, L.; Wang, Y.; Meng, M.; Jin, L.; Luo, X.; Chen, Y.; Li, X.; Xiao, S.; Wang, H.; Luo, Y.; Qiu, C.-W.; Duan, H. Trichromatic and tripolarization-channel holography with noninterleaved dielectric metasurface *Nano Lett.* **2019,** *20*, 994-1002.
35. Gerchberg, R. W. A practical algorithm for the determination of phase from image and diffraction plane pictures *Optik* **1972,** *35*, 237-246.
36. Guo, Q.; Schlickriede, C.; Wang, D.; Liu, H.; Xiang, Y.; Zentgraf, T.; Zhang, S. Manipulation of vector beam polarization with geometric metasurfaces *Opt. Express* **2017,** *25*, 14300-14307.
37. Goodman, J. W., *Introduction to Fourier optics*. Roberts and Company Publishers: 2005.
38. Khorasaninejad, M.; Chen, W. T.; Devlin, R. C.; Oh, J.; Zhu, A. Y.; Capasso, F. Metalenses at visible wavelengths: Diffraction-limited focusing and subwavelength resolution imaging *Science* **2016,** *352*, 1190-1194.
39. Wu, P. C.; Tsai, W. Y.; Chen, W. T.; Huang, Y. W.; Chen, T. Y.; Chen, J. W.; Liao, C. Y.; Chu, C. H.; Sun, G.; Tsai, D. P. Versatile Polarization Generation with an Aluminum Plasmonic Metasurface *Nano Lett.* **2017,** *17*, 445-452.
40. Chen, C.; Wang, Y.; Jiang, M.; Wang, J.; Guan, J.; Zhang, B.; Wang, L.; Lin, J.; Jin, P. Parallel Polarization Illumination with a Multifocal Axicon Metalens for Improved Polarization Imaging *Nano Lett.* **2020,** *20*, 5428-5434.
41. Deng, L.; Deng, J.; Guan, Z.; Tao, J.; Chen, Y.; Yang, Y.; Zhang, D.; Tang, J.; Li, Z.; Li, Z. Malus-metasurface-assisted polarization multiplexing *Light Sci. Appl.* **2020,** *9*, 1-9.
42. Deng, J.; Deng, L.; Guan, Z.; Tao, J.; Li, G.; Li, Z.; Li, Z.; Yu, S.; Zheng, G. Multiplexed anticounterfeiting meta-image displays with single-sized nanostructures *Nano Lett.* **2020,** *20*, 1830-1838.